Bidirectional Anions Gathering Strategy Afford Efficient Mixed Pb-Sn Perovskite Solar Cells

Yuli Tao, Zheng Liang, Jiajiu Ye, Huifen Xu, Guozhen Liu, Dmitry Aldakov, Xu Pan, Peter Reiss, Xingyou Tian

Bidirectional Anions Gathering Strategy Afford Efficient Mixed Pb-Sn Perovskite Solar Cells

Yuli Tao[1,2#], Zheng Liang[1#], Jiajiu Ye[1#], Huifen Xu[1], Guozhen Liu[1], Dmitry Aldakov[3], Xu Pan[1], Peter Reiss,[3]* Xingyou Tian[1]**

1. Key Laboratory of Photovoltaic and Energy Conservation Materials, Institute of Solid-State Physics, Hefei Institutes of Physical Science, Chinese Academy of Science, Hefei 230031, China.
2. University of Science and Technology of China, Hefei 230026, China.
3. Univ. Grenoble Alpes, CEA, CNRS, INP, IRIG/SyMMES, STEP, 38000 Grenoble, France

E-mail: xpan@rntek.cas.cn, peter.reiss@cea.fr, xytian@issp.ac.cn

Keywords: mixed Pb-Sn perovskite solar cells, bidirectional anions gathering strategy, ideal band gap, high efficiency, long-term stability

Abstract

Mixed lead-tin (Pb-Sn) perovskite solar cells (PSCs) possess low toxicity and adjustable bandgap for both single-junction and all-perovskite tandem solar cells. However, the performance of mixed Pb-Sn PSCs still lags behind the theoretical efficiency. The uncontrollable crystallization and the resulting structural defect are important reasons. Here, we report the bidirectional anions gathering strategy (BAG) by using Methylammonium acetate (MAAc) and Methylammonium thiocyanate (MASCN) as perovskite bulk additives, which Ac^- escapes from the perovskite film top surface while SCN^- gathers at the perovskite film bottom in the crystallization process. After the optoelectronic techniques, we demonstrate the bidirectional anions movement caused by the top-down gradient crystallization. The layer-by-layer crystallization will collect anions in the next layer and gather at the broader, enabling a controllable crystallization process, thus getting a high-quality perovskite film with better phase crystallinity and lower defect concentration. As a result, PSCs treated by the BAG strategy exhibited outstanding photovoltaic and electroluminescent performance with a champion efficiency of 22.14%. Additionally, it demonstrates excellent long-term stability, which retains around 92.8% of its initial efficiency after 4, 000 hours aging test in the N_2 glove box.

1. Introduction

Metal halide perovskite solar cells are a promising candidate for the next-generation photovoltaic technology with a record power conversion efficiency (PCE) of 25.7%.[1] According to the Shockley-Queisser (S-Q) limit, the potential PCE can be further pull-up by bringing the perovskite bandgap to the ideal range of ~1.3-1.4 eV.[2] However, the bandgap of traditional high-performance Pb-based perovskite materials is usually dispersed in the range of ~1.5-1.7 eV,[3] limiting the improvement of the potential. By making Pb-Sn compositions of partially replacing Pb with 20% content Sn, the perovskite bandgap can be adjusted to the ideal value, and it is a novel concept for further boosting PSCs theoretical efficiency expectation.[4]

However, introducing Sn into the perovskite lattice will adversely affect the film performance, resulting in the PCE of mixed Pb-Sn PSCs still far from the theoretical value.[5] Over fast and uncontrollable crystallization processes are the main reasons to take responsibility for the loss, which is attributed to the stronger reaction between Sn and organic components as Sn^{2+} has a higher Lewis acidity than Pb^{2+}.[6] As a result, it causes faster nucleation and growth rate as well as imperfect growth of perovskite film during the solution process.[7] Furthermore, the resulting defective perovskite grain can trigger off the trap-state generation and Sn^{2+} oxidation, degrading device efficiency and stability.[8,9] Therefore, it is imperative to manipulate the crystallization process for obtaining high-quality mixed Pb-Sn perovskite film.

Lots of efforts have been devoted to studying the perovskite crystal nucleation and crystal growth mechanisms, expecting to regulate the mixed Pb-Sn perovskite crystallization process. Zhang et al. introduced caffeic acid into the mixed Pb-Sn perovskite precursor solution, indicating the antioxidant caffeic acid can effectively adjust the nucleation energy barrier and slow down the crystal growth rate.[10] Shuzi Hayase et al. found the addition of RbI and KI can improve the grain compactness, crystallinity, and crystal preferential orientation growth in mixed Pb-Sn perovskite film.[11] To form highly crystalline 3D mixed Pb-Sn perovskites, Maria Antonietta Loi et al. deposited a 2D perovskite template as the nucleus, which was then converted in situ to a crystal structure with a highly stoichiometric ratio and (001) planes orientation.[12] Besides, the temperature of antisolvent also has a significant impact on nucleation. Yan et al. demonstrated that the cold antisolvent treatment can reduce the nucleation density and slow down the nucleation rate of mixed Pb-Sn perovskite, while hot antisolvent increases nucleation sites.[13]

The above methods can improve mixed Pb-Sn PSCs performance but are still less effective because of the unexpected crystallization and defective grain. It can be learned from previous research, that with the evaporation of residual solvent from the top surface during the perovskite film annealing period, the perovskite film follows the downward growth from the intermediate phase.[14,15,16] The intermediate phase is formed by coordinating perovskite precursor with additive or solvent before forming the final films, which is closely related to the coordination ability between Pb^{2+}/Sn^{2+} and coordination compounds.[17] Such an intermediate phase serves as a template to modulate the downward crystal growth, thus effectively retard the rapid growth of perovskite grains.

Besides, introducing volatile amine salts could benefit crystal growth because the ions would first anchor onto the liquid-gas interface as a nucleation agent with (001)-preferred orientation.[18] Liu et al. also suggested that the role of some volatile substances plays more like a solvent rather than a common passivation additive.[19] Consequently, manipulating the gradient crystal growth through highly coordinated ability compounds and the evaporation of volatile salt may be a reasonable method.

Here, we reported a new strategy to manipulate mixed Pb-Sn perovskite growth, which employed MAAc and MASCN as perovskite bulk additives in the precursor solution. Because MAAc is volatile salt and SCN^- has a strong coordination ability to form the intermediate phase with Pb^{2+}/Sn^{2+}.[20,21,22,23] With the residual solvent evaporating from perovskite film during the annealing process, the Ac^- would escape from the top surface since MAAc is thermally unstable and easily decomposed by heating. Meanwhile, as the layer-by-layer gradient crystallization original from the top layer template, the SCN^- with certain mobility that did not enter into the lattice, will move to the grain boundary (GB) or move down, and finally gather at the perovskite film bottom (**Figure 3**h). After several optoelectronic techniques analyses, we demonstrated that the bidirectional movement of the two anions will enable the perovskite crystallization with a controllable process, thus getting a high-quality perovskite film with better phase crystallinity and low defect concentration. As a result, we got simultaneous improvement in both open-circuit voltage (V_{OC}, 0.88 V) and fill factor (FF, 80.06%) of the BAG-device, resulting in a champion device efficiency of 22.14%. Remarkably, it showed great long-term stability, maintaining around 92.8% of its initial efficiency after 4, 000 hours aging test. These findings provided a simple and practicable strategy to manipulate perovskite growth for better optoelectronic performance.

2. Results and discussion

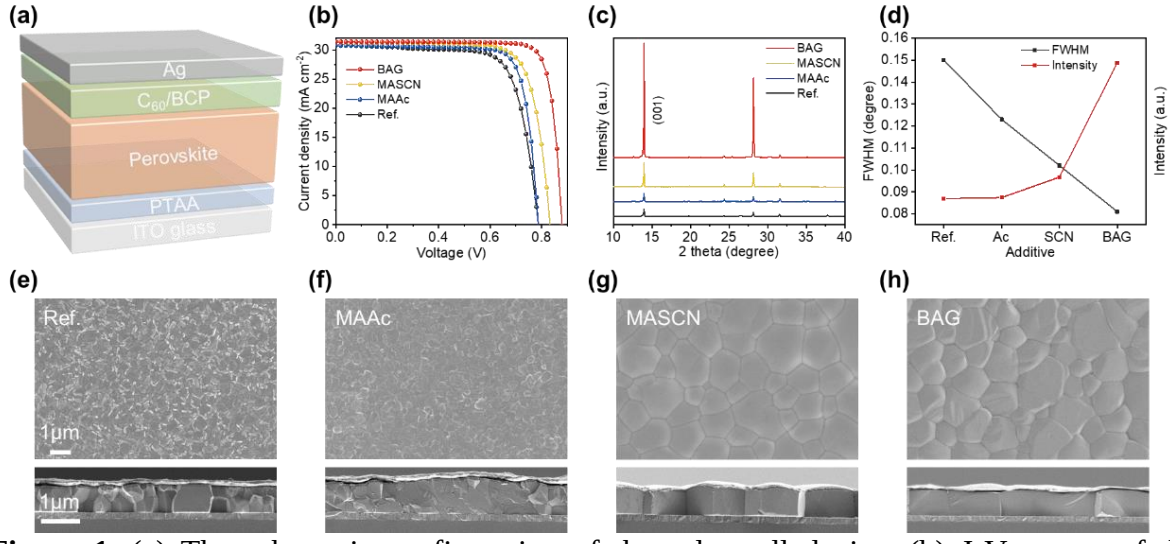

Figure 1. (a) The schematic configuration of the solar cell device. (b) J-V curves of the champion devices fabricated with different additives. (c) XRD pattern of perovskite films with different additives. (d) FWHM and XRD intensity were obtained from the (001) crystal plane of XRD patterns. (e-h) Top-view SEM images and cross-section SEM images of (e) reference film, (f) MAAc-film, (g) MASCN-film, (h) BAG-film. The scale bar is 1 μm.

The solar devices were fabricated with an inverted p-i-n configuration of ITO glass/ PTAA/ Perovskite/ C_{60}/ BCP/ Ag (**Figure 1**a) and details of device preparation are provided in the

device fabrication section. The formula of reference perovskite molecular is $(FAPbI_3)_{0.8}(MASnI_3)_{0.2}$ and treated with the BAG strategy, which employed MAAc and MASCN as co-modifier. Meanwhile, separately MAAc and MASCN were employed in the perovskite precursor solution for cross-reference. **Figure 1**b shows the current density-voltage (J-V) curves of the best-performing PSCs of different ammonium salt treatments under AM 1.5 G simulated solar illumination, and the corresponding photovoltaic parameters are listed in **Support Table 1**. The champion device treated by the BAG strategy yielded a PCE of 22.14% with a V_{OC} of 0.88 V, a short-circuit current density (J_{SC}) of 31.42 mA cm^{-2} and an FF of 80.06%. In contrast, the reference device exhibited a much lower PCE of 17.87% with a V_{OC} of 0.78 V, a J_{SC} of 30.89 mA cm^{-2}, and an FF of 73.53%. We verify the J_{SC} by EQE measurement (**Figure S1**), the integrated J_{SC} was 29.03 mA cm^{-2} and 30.05 mA cm^{-2} for the reference and BAG-devices, respectively, which is compatible with the J-V scan. Owning to the synergistic effect between the two molecules, the BAG-device showed superior performance compared with both MAAc-device and MASCN-device.

X-ray diffraction (XRD) was carried out to investigate the origin of this increase in PCE. As can be seen in **Figure 1**c, XRD measurement showed peak positions at around 12.75° and 13.98° for reference films, corresponding to the PbI_2 and perovskite (001) crystal plane, respectively.[24] Notably, with the BAG strategy, the characteristic perovskite reflection peak intensity is almost 16 times that of the reference and much higher than that of MAAc-film and MASCN-film. Subsequently, we evaluated crystallinity through full width at half maximum (FWHM) obtained from the (001) crystal plane of XRD patterns (**Figure 1**d). With the BAG strategy, the FWHM value narrows down from 0.150° to 0.081°, indicating improved crystallinity of the perovskite film.[25] In addition, these two anions work as co-passivate which affected crystallization kinetics during the stage of perovskite film formation, rather than altering the crystal structure of the perovskite films. Because the ionic radius of Ac^- (0.162 nm) and SCN^- (0.217 nm) are both smaller than that of I^- (0.220 nm), crystal lattice parameters would decrease if SNC^- or Ac^- is incorporated in the lattice.[16] However, neither shifts in the peaks, nor new peaks are observed in the XRD patterns (**Figure S2**).

From the top-view and cross-section SEM images (**Figure 1** (e-h)), we observed the reference perovskite film manifested a small grain size with a substantial number of grain boundaries. This phenomenon has been extensively reported due to the fast crystallization during the film deposition process.[26,27,28] Commonly, a large number of defects are inevitably formed at the grain boundary, which served as non-radiative recombination centers and caused energy loss.[29] Therefore, a perovskite film with large grains and fewer grain boundaries is crucial for high-performance solar cells. With the incorporation of MASCN, grain size increases dramatically. However, the film roughness average (Ra) improved (21.4 nm for reference film and 36.8 nm for MASCN-film) as shown in the atomic force microscopy images (AFM, **Figure S7**). Surprisingly, the film roughness of MAAc-film is 18.5 nm. And as add MASCN and MAAc in the precursor solution at the same time (BAG strategy), the Ra decreased to 23.9 nm, which indicated Ac^- has a role in improving the film flatness. A high-quality film with a large grain size and smooth surface is expected to reduce the density of trap states significantly. As observed from the cross-section SEM, perovskite grains of the BAG-film showed highly ordered stacking with monolithic columnar crystal from the top to the bottom, leading to decreased grain boundary along the vertical direction. All in all, the BAG-film with high crystallinity, large grain, and smooth surface enables low structure defects and is expected to be beneficial for charge carrier transport and extraction.[30]

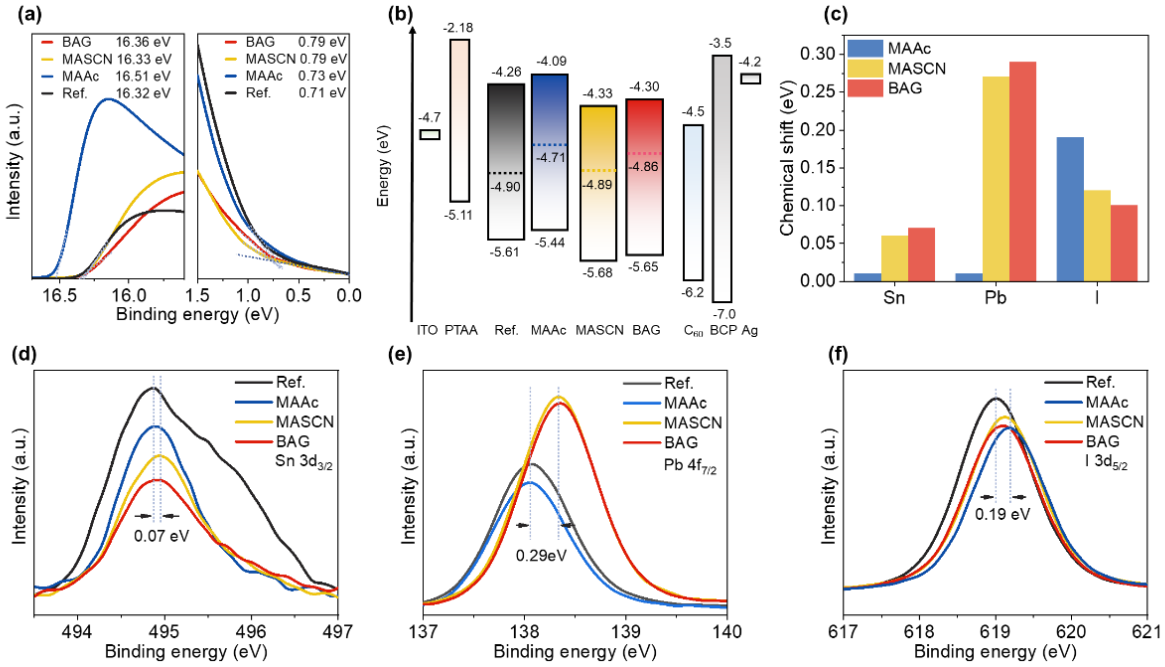

Figure 2. (a) UPS spectra of secondary electron cutoff and valence band of the perovskite films. (b) Energy-level scheme based on the parameters calculated from UPS spectra. (c) Chemical shift statistics of Sn $3d_{3/2}$, Pb $4f_{7/2}$, and I $3d_{5/2}$ of perovskite films with different additives. (d-f) Comparative studies on the positions of the (d) Sn $3d_{3/2}$, (e) Pb $4f_{7/2}$, and (f) I $3d_{5/2}$ XPS peaks.

Ultra-violet photoelectron spectroscopy (UPS) and UV-vis absorption spectroscopy were performed to evaluate the energy level alignment between perovskite film and charge transport layer, which strongly affected V_{OC} loss and charge carrier transmission capacity.[31] By subtracting the binding energy of the secondary edge (16.32 eV, 16.51 eV, 16.33 eV, 16.36 eV) of different films (reference film, MAAc-film, MASCN-film, BAG-film) from the excitation energy of the UV photons (21.22 eV, He I UPS) spectra (**Figure 2**a), the Fermi energy (E_f) is estimated to be -4.90 eV, -4.71 eV, -4.89 eV, and -4.86 eV, respectively. From the UPS cutoff levels, the energy difference between the valence band maximum (VBM) and the Fermi level is estimated to be 0.71 eV, 0.73 eV, 0.79 eV, and 0.79 eV, resulting in VBM is -5.61 eV, -5.44 eV, -5.68 eV, and -5.65 eV, for samples of reference film, MAAc-film, MASCN-film, and BAG-film, respectively. As demonstrated by the Tauc plots (**Figure S8**) from UV-vis spectra,[32] the optical bandgap of the perovskite film is 1.35 eV. Therefore, the conduction band minimum (CBM) levels are calculated as -4.26 eV, -4.09 eV, -4.33 eV, and -4.30 eV, for samples of reference film, MAAc-film, MASCN-film, and BAG-film, respectively. The band level diagram of devices is constructed in **Figure 2**b. The CBM of BAG-film shifts downward for 0.04 eV, causing a smaller energy gap with the LUMO of C_{60} (-4.5 eV) and better energy alignment.[33] Additionally, the BAG strategy results in the lifting of the perovskite Fermi level that gives rise to a larger built-in voltage, which can supply a larger driving force to separate the electrons and holes, thus minimizing the V_{OC} loss.

X-ray photoelectron spectroscopy (XPS) measurement was carried out to explore atom chemical environment change and potential bonding of perovskite, aiming to find out the synergistic effect of SCN^- and Ac^- anion with perovskite component (**Figure 2(**d-f), and **Figure S10**).[34] XPS peak of the reference film locates at 494.86 eV (for Sn $3d_{3/2}$) and 138.04 eV (for Pb $4f_{7/2}$), and the chemical shift value with different additives in Sn $3d_{3/2}$ (**Figure 2**d) and Pb $4f_{7/2}$ (**Figure 2**f) spectra were further analyzed. In Sn $3d_{3/2}$ XPS spectra (**Figure 2**d), the difference between reference film and MAAc-film, MASCN-film, and BAG-film are not remarkable. In contrast, the peak binding energy of the Pb $4f_{7/2}$ spectrum exhibits a clear shift

toward higher binding energy (~0.29 eV) for MASCN-film and BAG-film, whereas 0.08 eV for MAAc-film**,** indicating Pb-containing structure octahedral is favored anchored with SCN^- anion. As for the XPS pattern of I $3d_{5/2}$ (**Figure 2**e), the MAAc-film exhibits the highest shift by about 0.19 eV, which may be due to the polar hydrogen group (OH-) of Ac^- and the electronegative iodide ion ($I^{\delta-}$) can form hydrogen bonding. The hydrogen bonding can suppress the migration of I^- and the oxidation of I^- to I_2 or I_3^-, guarantees the stoichiometric ratio of perovskite, and reduce iodine vacancy defects. **Figure 2**d shows the chemical shift statistics of Sn $3d_{3/2}$, Pb $4f_{7/2}$, and I $3d_{5/2}$ of different additives.[35]

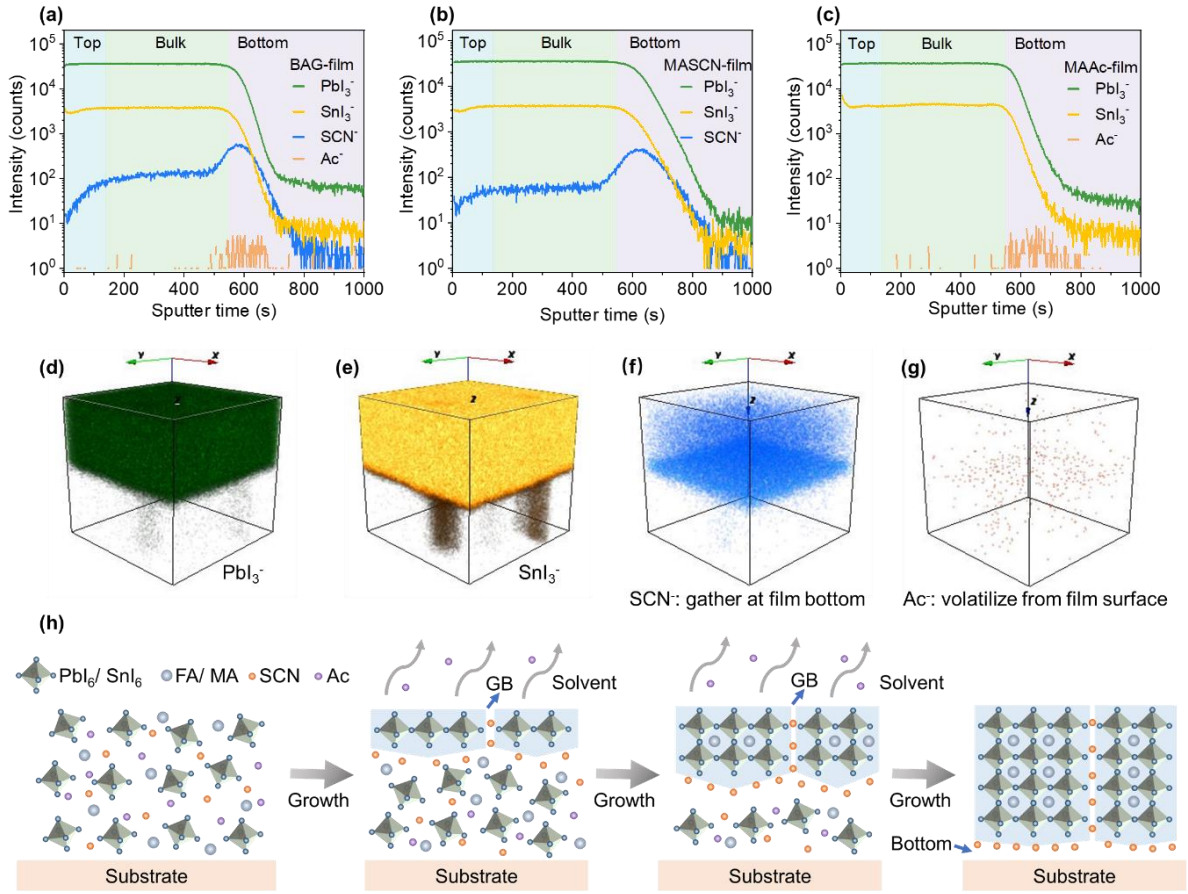

Figure 3. (a-c) TOF-SIMS depth profiles of (a) BAG-film, (b) MASCN-film, and (c) MAAc-film. (d-f) The 3D maps obtained from BAG-film show the distribution of (d) PbI_3^-, (e) SnI_3^-, (f) SCN^-, and (g) Ac^-. (h) Illustration of the dynamic distribution of Ac^- and SCN^- during the gradient crystallization process of BAG perovskite, in which Ac^- escapes from the surface while SCN^- moves to GB or moves down.

Time-of-flight secondary ion mass spectroscopy (TOF-SIMS) measurement was performed to probe the depth profile of perovskite film.[36] As shown in **Figure 3**(a), the depth profiles of the BAG-film exhibit that PbI_3^- and SnI_3^- signals are almost constant throughout the film with a uniform distribution. However, the SCN^- signal distributes throughout the surveyed depth and accumulates at the film bottom. The corresponding three-dimensional (3D) maps of BAG-film were shown in **Figures 3**(d-g) and clearly exhibit that SCN^- is located in the perovskite film bottom (**Figure 3**f). As SCN^- did not enter the crystal lattice from our previous discussion, we reasonably consider the SCN^- would exist in the grain boundary or film bottom. Notably, though the BAG precursor solution has the same concentration of MASCN and MAAc, the distribution of the two anions shows a great difference after annealing. There is almost no Ac^- signal (**Figure 3**g) in TOF-SIMS depth profiles. From the FTIR spectra of the perovskite film (**Figure S11**),

there is no difference between BAG-film, MASCN-film, MAAc-film, and Ref.-film, which indicates the near absence of Ac^- in the BAG-film. In addition, we also tested the MASCN-film and MAAC-film by TOF-SIMS test separately (**Figure 3**b, **3**c), and the distribution of PbI_3^-, SnI_3^-, SCN^-, and AC^- show the same trend compared with BAG-film.

Based on XRD measurement, XPS measurement, TOF-SIMS analysis, and previous reports, the mechanism and gradient crystallization process of BAG-film may undergo the following process during the annealing time. With the evaporation of residual solvent from the surface during the perovskite film annealing period, the volatile salts MAAc can activate the precursor solution system to migrate fast and escape from the perovskite top surface, resulting in high flatness film with improved orientation. Simultaneous, with the upper part of the film (layer n, layer n-1, …) transformed from the SCN^- related intermediate phase to the perovskite phase, SCN^- will be separated from the intermediate phase and move downward to the next layer. The process is repeated until perovskite layers are completely formed, and finally leads to the absence of Ac^- in the film and enrichment of SCN^- anion at the perovskite film bottom. As a result, with the synergetic effect of the Ac^- escape from the top surface and the SCN^- move downward, perovskite grain growth was precisely controlled and high-quality perovskite film was got, giving an increase in grain size and improved phase crystallinity. Moreover, Sang Il Seok et al. pointed out that perovskite film bottom has higher defect concentration than bulk and top surface.[37] Thus, SCN^- with overall spatial distribution and accumulation at the bottom interface could passivate the defects effectively.

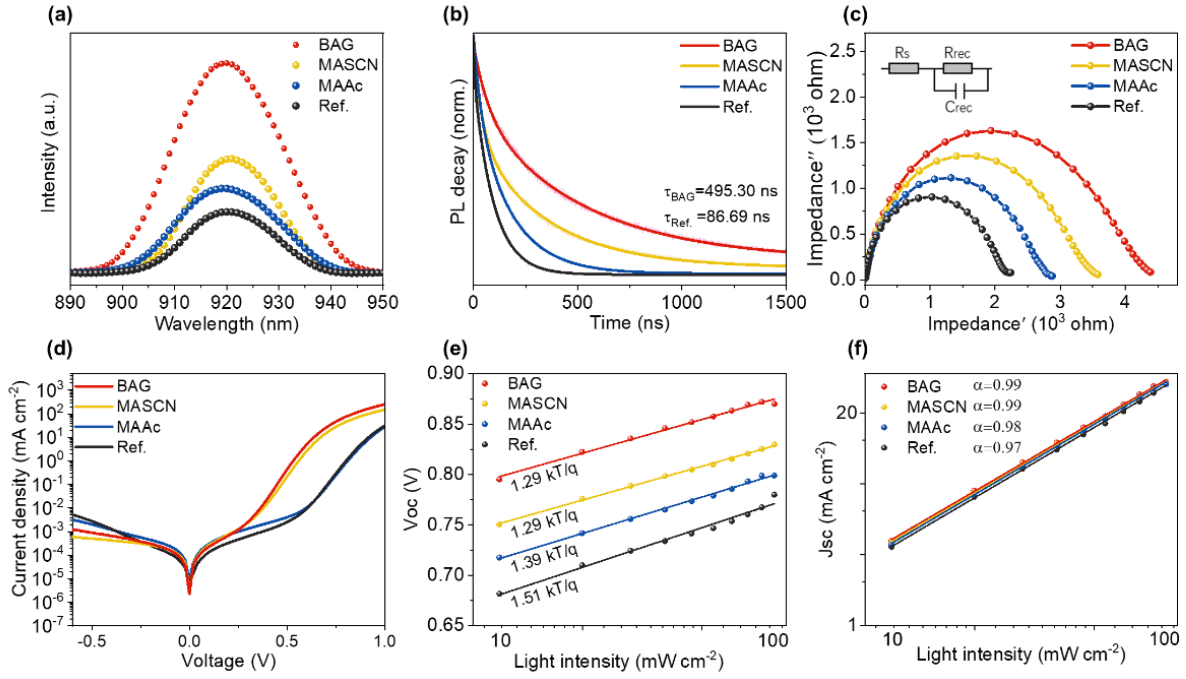

Figure 4. (a) Steady-state PL spectra of perovskite films deposited on glass. (b) TRPL decay profiles of perovskite films deposited on glass. (c) Nyquist plots of PSCs. The inset picture was an equivalent circuit. (d) J-V curves of the devices under dark conditions. (d) V_{OC} dependency on the light intensity and linear fitted slope. (e) J_{SC} dependency on the light intensity and linear fitted slope.

Charge carrier transport and recombination are strongly related to crystal quality.[38] Therefore, after obtaining high-quality perovskite film, we systematically investigated the charge carrier transfer and recombination kinetics. Steady-state PL measurements were collected from the perovskite films deposited on glass and the corresponding curves are shown in **Figure 4**a. The highest PL intensity is found in BAG-film, indicating a high crystal quality, in agreement with

the XRD pattern and SEM images.[39] From time-resolved PL (TRPL) measurements, the carrier lifetime value obtained from BAG-film is extended by six times that of the reference (**Figure 4**b). Long carrier lifetimes imply a reduction in trap density dispersed at the grain boundaries and polycrystalline perovskite film surfaces.[40] Specific parameters can be obtained from **Support Table 2**. Furthermore, to comprehensively investigate the influence of BAG strategy on the charge transfer behavior, electronic impedance spectroscopy (EIS) characterization was performed. **Figure 4**c represented Nyquist plots of devices, and the equivalent circuit model is shown in the inset. The single semicircle of Nyquist plots represents charge recombination resistance values (R_{rec}). It can be concluded that the BAG-device shows a larger R_{rec} than the reference, which is mainly attributed to fewer defect-assisted traps to restrain the charge recombination.[41] It was also proved from the dark J-V curves (**Figure 4**d), that the dark current density of the BAG-device is almost reduced by one order of magnitude than reference because of the enhancing flatness and fewer pinholes, resulting in lower leakage current in the dark J-V curves.[42] Dependences of device voltage and current on illumination intensity were carried out to further evaluate carrier recombination kinetic (**Figure 4**e, **4**f).[43] **Figure 4**e shows the plots of V_{OC} versus illumination intensity. The slope of light intensity-dependent V_{OC} curves represents the degree of non-radiative recombination progress, where the deviation of 1 kT/q indicates the possibility of trap-assisted recombination under open-circuit conditions (k is the Boltzmann constant, T is the Kelvin temperature, and q is the elementary charge). The BAG-device demonstrates a slope of 1.29 kT/q, which is smaller than that of the reference device (1.51 kT/q), revealing carrier recombination has largely been suppressed. The double logarithmic plot of J_{SC} and illumination intensity accords with the power rate relationship of $J_{SC} \propto I\alpha$, where α is the exponential factor. Compared to the reference devices, the exponent α for the BAG-devices incorporated device is closer to 1 (**Figure 4**f), which proves less bimolecular recombination. The above results further approve that the BAG strategy can effectively suppress their recombination and promote effective carrier transfer.

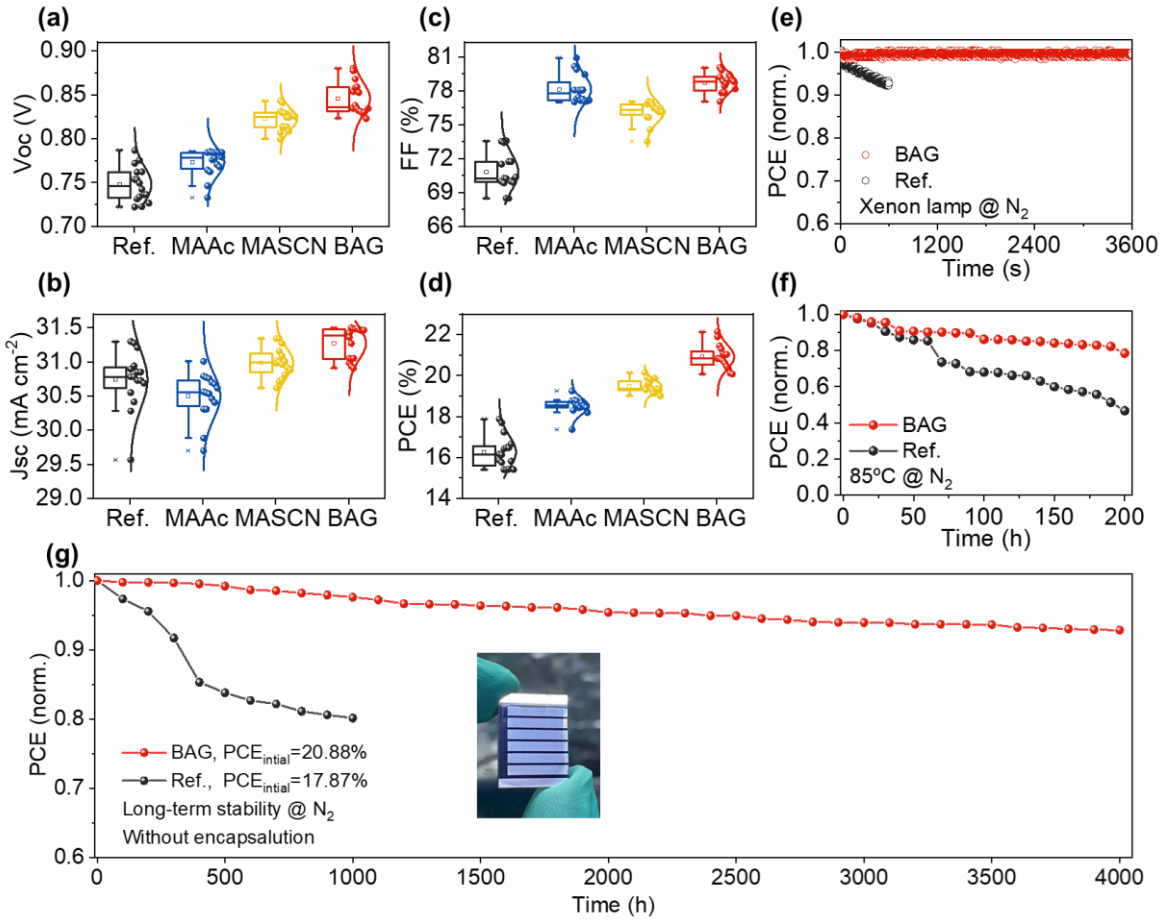

Figure 5. (a-d) Distribution of (a) V_{OC}, (b) J_{SC}, (c) FF, and (d) PCE. (e-g) Stability of the reference device and BAG-device which were stored in the N_2 glovebox without encapsulation: (e) MPP tracking of normalized PCE at continuous Xenon lamp light irradiation, (f) thermal stability of normalized PCE under 85 °C, (g) long-term stability of normalized PCE and the inset shows a device photograph.

The statistical distributions of photovoltaic parameters of the solar cells (16 devices) are given in **Figure 5**a, **5**b, **5**c, and **5**d. The best V_{OC} of reference devices was 0.79 V, whereas the MASCN-devices showed a V_{OC} of 0.83 V, indicating SCN^- can effectively improve the V_{OC}. However, the rough topography was got deteriorated and series resistance was increased as SCN^- introduced, resulting in low FF in MASCN-devices. As for MAAc-devices, V_{OC} gets slightly increased while the enhanced FF was observed, owing to the improved film flatness. Though both MAAc and MASCN have shown some favorable contributions to the perovskite film, just using either of them as a single additive is hard to achieve satisfying performance. Overall, the BAG-devices showed improved performance across all photovoltaic parameters and led to a higher PCE. Through the synergy of the bimolecular, each molecule sticks to its post, and finally, the device performance got substantially improved.

The irreversible degradation of PSCs driven by moisture, heat, and light starts from the defective state of the grain boundary and film interface, and gradually spreads to the grain bulks. Device stability was conducted by testing power output stability, thermal stability, and long-term stability. With the BAG strategy, a high crystallinity uniform film with less grain boundaries can be obtained, which is expected to reduce the density of trap states significantly. As shown in **Figure 5**e, the maximum power point (MPP) tracking at continuous Xenon lamp light irradiation was tested, and the BAG-device showed a nearly unchanged PCE under 3600

seconds while the reference device decreased to 80% of its initial value within 600 seconds. Then, we tracked the thermal stability of PSCs under the temperature of 85 °C. BAG-device retained 78.5% of initial efficiency after 200 hours, much higher than reference devices (below 50%). We further measured the long-term stabilities of devices, which were conducted in the N_2 glove box. Similar to the previous stability test, the reference device exhibited rapid reduction, and the PCE (17.87%) decreased to 80.1% of its initial value after 1, 000 hours aging test. In contrast, the BAG-device showed a much slower PCE decrease and kept 92.8% of the initial PCE (20.88%) at least 4, 000 hours aging test. The impressive stability increase originated from the defect at the grain boundary or film bottom was passivated and high-quality films were shaped. And the phenomenon further proved the superiority of the BAG strategy by using SCN^- and Ac^- in mixed Pb-Sn PSCs.

3. Conclusion

In summary, we have developed a novel and effective bidirectional anion mobile strategy, by using MAAc and MASCN as additives in the perovskite precursor solution, to improve the mixed Pb-Sn perovskite film quality. During the top-down growth process of the perovskite film, with the evaporation of the residual solvent, the volatile salt MAAc will escape from the top surface, whereas the SCN^- will move to the grain boundary or move down. With the synergetic effect of the two anions, we found that the bidirectional movement of the two anions will enable the crystallization with a controllable process, thus getting a high-quality perovskite film with a lower defect concentration. Finally, we got a competitive efficiency of 22.14%. Notably, it showed great long-term stability, maintaining around 92.8% of its initial efficiency after 4, 000 hours aging test. We expected that our new strategy can be widely recognized and help researchers to achieve high performance of mixed Pb-Sn perovskite solar cells

4. Experimental Section/Methods

Materials

Lead iodide (PbI_2, 99.999%), tin iodide (SnI_2, 99.999%), and tin fluoride (SnF_2, 99%) were purchased from Alfa Assar. N, N-dimethylformamide (DMF, 99.8%), dimethyl sulfoxide (DMSO anhydrous, 99.9%), chlorobenzene (CB anhydrous, 99.8%), isopropyl alcohol (IPA anhydrous, 99.8%) and (2,3,5,6-Tetrafluoro-2,5-cyclohexadiene-1,4-diylidene) dimalononitrile (F_4-TCNQ, 97%) were purchased from Sigma Aldrich. Formamidinium iodide (FAI) and methylammonium iodide (MAI) were purchased from Liaoning Advanced Election Technology CO. Ltd., China. Poly(triaryl)amine (PTAA), fullerene (C_{60}), and bathocuproine (BCP) were bought from Xi'an Polymer Light Technology Co. Ltd., China. Methylammonium Thiocyanate (MASCN, 95.0%) was bought from Aladdin, China. Methylamine Acetate (MAAc, 98%) was bought from TCI. Ethylenediamine diiodide (EDAI, 98%) and phenethylammonium

iodide (PEAI, 98%) were purchased from TCI. All the chemical reagents were used in the experiments without any further purification.

Device fabrication

ITO glass substrates ((7Ω square^{-1}) were washed sequentially with detergent, deionized water, acetone, and isopropanol in an ultrasonic bath system for 15 minutes. Then, the ITO glasses were dried by an air gun. Before use, the ITO glass was treated with an ultraviolet-ozone system for 20 minutes to improve the glass wettability and transferred into the N_2 glove box. We first made a stock solution of F_4-TCNQ in CB (0.2 mg ml^{-1}), which was stirred at 60 °C for 12 hours. F_4-TCNQ solution was then added into PTAA solution (2 mg ml^{-1} in CB) with a weight ratio of 1%. 85 μl F_4-TCNQ-doped PTAA solution was spin-coated onto the ITO substrates at 6, 000 rpm for 30 seconds followed by heating at 100 °C for 15 minutes. Before deposition of perovskite solution, the PTAA-coated ITO substrates were pre-treated by spin-coating 85 μl DMF at a speed of 5, 000 rpm for 30 seconds to improve wettability.

1.6 M mixed Pb-Sn perovskite precursor solution for reference film was prepared by adding 220.1 mg FAI, 590.1 mg PbI_2, 50.9 mg MAI, 119.2 mg SnI_2, 5 mg SnF_2 (as an antioxidant to suppress oxidation of tin) in the mixed solvent of DMF: DMSO (4: 1 volume ratio, 1 ml). The BAG-perovskite precursor solution was dissolving 14.4 mg MASCN (0.16 M) and 14.6 mg MAAc (0.16 M) in 1 ml reference perovskite precursor solution. The MASCN-perovskite precursor solution was dissolving 14.4 mg MASCN (0.16 M) in 1 ml reference perovskite precursor solution. The MAAc-perovskite precursor solution was dissolving 14.6 mg MAAc (0.16 M) in 1 ml reference perovskite precursor solution. The obtained solution was stirred for 12 hours and filtered by a 0.22 μm Polytetrafluoroethylene (PTFE) filter before use. Then 160 μl perovskite precursor solution was spun at 1, 000 rpm for 10 seconds followed by 4, 000 rpm for 40 seconds, where 200 μl CB was dropped onto the center of the spinning substrate at 40th second. The film was immediately annealed at 100 ℃ for 10 minutes.

1.5 mg EDAI is added to 1 ml IPA and stirred for over 2 hours at room temperature, followed by filtered by a 0.22 μm PTFE filter to obtain EDAI solution. Then 3 mg PEAI was added to 1 ml EDAI solution and stirred for 1 hour as a post-treatment solution. 85 μl post-treatment was deposited onto perovskite films by spin-coating at 3, 000 rpm for 30 seconds, followed by annealing at 100 ℃ for 5 minutes. The devices were completed by thermally evaporating 25 nm C_{60}, 7 nm BCP, and 100 nm Ag under a high vacuum system. The mixed Pb-Sn perovskite

film deposition is highly sensitive to O_2 concentration. In the device fabrication process, the O_2 concentration was controlled under 0.01 ppm.

Characterizations

The J-V measurement was measured by using a xenon lamp based solar simulator (Enlitech, SS-F5-3A, Class AAA) and a source meter (Keysight B2901A, USA). The simulated AM 1.5G irradiation (100 mW cm^{-2}) was calibrated by a standard silicon cell (certified by NREL, SRC-2020). The device area of 0.0625 cm^2 was defined by a metal mask to accurately define the active area. We test the solar cell in N_2 glove box with a temperature of 25±2 ℃.

Acknowledgements

The authors gratefully acknowledge the financial support from the National Key R&D Program of China (No.2021YFB3800102), the Science Funds of Distinguished Young Scholars of Anhui Province (Grant No. 2108085J34) and the Key Lab of Photovoltaic and Energy Conservation Materials, Chinese Academy of Sciences (Grant No. PECL2021QN002).

# contributed equally to this work

Received: ((will be filled in by the editorial staff))
Revised: ((will be filled in by the editorial staff))
Published online: ((will be filled in by the editorial staff))

References

1. Best Research-Cell Efficiency Chart, https://www.nrel.gov/pv/cellefficiency.html (accessed: January 2023).

2. Wu, T., Liu, X., Luo, X., Lin, X., Cui, D., Wang, Y., ... & Han, L. (2021). *Joule*, *5*(4), 863-886.

3. Klug, M. T., Milot, R. L., Patel, J. B., Green, T., Sansom, H. C., Farrar, M. D., ... & Snaith, H. J. (2020). *Energy & Environmental Science*, *13*(6), 1776-1787.

4. Liang, Z., Xu, H., Zhang, Y., Liu, G., Chu, S., Tao, Y., ... & Ye, J. (2022). *Advanced Materials*, 2110241.

5. Hu, S., Otsuka, K., Murdey, R., Nakamura, T., Truong, M. A., Yamada, T., ... & Wakamiya, A. (2022). *Energy & Environmental Science*, *15*(5), 2096-2107.

6. Jiang, X., Li, H., Zhou, Q., Wei, Q., Wei, M., Jiang, L., & Ning, Z. (2021). *Journal of the American Chemical Society*, *143*(29), 10970-10976.

7. Lim, E. L., Hagfeldt, A., & Bi, D. (2021). *Energy & Environmental Science*, *14*(6), 3256-3300.

8. Ni, Z., Bao, C., Liu, Y., Jiang, Q., Wu, W. Q., Chen, S., ... & Huang, J. (2020). *Science*, *367*(6484), 1352-1358.

9. Lanzetta, L., Webb, T., Zibouche, N., Liang, X., Ding, D., Min, G., ... & Haque, S. A. (2021). *Nature communications*, *12*(1), 1-11.

10. Liu, H., Wang, L., Li, R., Shi, B., Wang, P., Zhao, Y., & Zhang, X. (2021). *ACS Energy Letters*, *6*(8), 2907-2916.

11. Sahamir, S. R., Kamarudin, M. A., Ripolles, T. S., Baranwal, A. K., Kapil, G., Shen, Q., ... & Hayase, S. (2022). *The Journal of Physical Chemistry Letters*, *13*(13), 3130-3137.

12. Xi, J., Duim, H., Pitaro, M., Gahlot, K., Dong, J., Portale, G., & Loi, M. A. (2021). *Advanced Functional Materials*, *31*(46), 2105734.

13. Cao, J., Loi, H. L., Xu, Y., Guo, X., Wang, N., Liu, C. K., ... & Yan, F. (2022). *Advanced Materials*, *34*(6), 2107729.

14. Chen, S., Xiao, X., Chen, B., Kelly, L. L., Zhao, J., Lin, Y., ... & Huang, J. (2021). *Science Advances*, *7*(4), eabb2412.

15. Chen, S., Dai, X., Xu, S., Jiao, H., Zhao, L., & Huang, J. (2021). *Science*, *373*(6557), 902-907.

16. Zheng, Y., Wu, X., Liang, J., Zhang, Z., Jiang, J., Wang, J., ... & Chen, C. C. (2022). *Advanced Functional Materials*, 2200431.

17. Xiang, W., Zhang, J., Liu, S. F., Albrecht, S., Hagfeldt, A., & Wang, Z. (2021). *Joule*.

18. Yan, N., Ren, X., Fang, Z., Jiang, X., Xu, Z., Zhang, L., ... & Liu, S. (2022). *Advanced Functional Materials*, 2201384.

19. Wu, G., Li, H., Cui, J., Zhang, Y., Olthof, S., Chen, S., ... & Liu, S. (2020). *Advanced Science*, *7*(10), 1903250.

20. Chen, J., & Park, N. G. (2021). *Small Methods*, *5*(6), 2100311.

21. Lian, X., Chen, J., Zhang, Y., Qin, M., Li, J., Tian, S., ... & Chen, H. (2019). *Advanced Functional Materials*, *29*(5), 1807024.

22. Yu, D., Wei, Q., Li, H., Xie, J., Jiang, X., Pan, T., ... & Ning, Z. (2022). *Angewandte Chemie International Edition*, *61*(20), e202202346.

23. Lu, H., Liu, Y., Ahlawat, P., Mishra, A., Tress, W. R., Eickemeyer, F. T., ... & Grätzel, M. (2020). *Science*, *370*(6512), eabb8985.

24. Luo, D., Yang, W., Wang, Z., Sadhanala, A., Hu, Q., Su, R., ... & Zhu, R. (2018). *Science*, *360*(6396), 1442-1446.

25. Sanchez-Diaz, J., Sánchez, R. S., Masi, S., Krecmarová, M., Alvarez, A. O., Barea, E. M., ... & Mora-Seró, I. (2022). *Joule*, *6*(4), 861-883.

26. Li, C., Song, Z., Chen, C., Xiao, C., Subedi, B., Harvey, S. P., ... & Yan, Y. (2020). *Nature Energy*, *5*(10), 768-776.

27. Peng, C., Li, C., Zhu, M., Zhang, C., Jiang, X., Yin, H., ... & Zhou, Z. (2022). *Angewandte Chemie*, e202201209.

28. Zhou, X., Zhang, L., Wang, X., Liu, C., Chen, S., Zhang, M., ... & Xu, B. (2020). *Advanced Materials*, *32*(14), 1908107.

29. Chen, B., Rudd, P. N., Yang, S., Yuan, Y., & Huang, J. (2019). *Chemical Society Reviews*, *48*(14), 3842-3867.

30. Fu, L., Li, H., Wang, L., Yin, R., Li, B., & Yin, L. (2020). *Energy & Environmental Science*, *13*(11), 4017-4056.

31. Kim, H., Lee, J. W., Han, G. R., Kim, Y. J., Kim, S. H., Kim, S. K., ... & Oh, J. H. (2022). *Advanced Functional Materials*, *32*(12), 2110069.

32. Wang, C., Zhang, Y., Gu, F., Zhao, Z., Li, H., Jiang, H., ... & Liu, Z. (2021). *Matter*, *4*(2), 709-721.

33. Xu, L., Feng, X., Jia, W., Lv, W., Mei, A., Zhou, Y., ... & Huang, W. (2021). *Energy & Environmental Science*, *14*(8), 4292-4317.

34. Ye, T., Wang, X., Wang, K., Ma, S., Yang, D., Hou, Y., ... & Priya, S. (2021). *ACS Energy Letters*, *6*(4), 1480-1489.

35. Su, Y., Yang, J., Liu, G., Sheng, W., Zhang, J., Zhong, Y., ... & Chen, Y. (2022). *Advanced Functional Materials*, *32*(12), 2109631.

36. Min, H., Kim, M., Lee, S. U., Kim, H., Kim, G., Choi, K., ... & Seok, S. I. (2019). *Science*, *366*(6466), 749-753.

37. Min, H., Lee, D. Y., Kim, J., Kim, G., Lee, K. S., Kim, J., ... & Il Seok, S. (2021). *Nature*, *598*(7881), 444-450.

38. Wang, J., Gao, Z., Yang, J., Lv, M., Chen, H., Xue, D. J., ... & Yang, S. (2021). *Advanced Energy Materials*, *11*(39), 2102131.

39. Meng, X., Lin, J., Liu, X., He, X., Wang, Y., Noda, T., ... & Han, L. (2019). *Advanced Materials*, *31*(42), 1903721.

40. Yang, X., Fu, Y., Su, R., Zheng, Y., Zhang, Y., Yang, W., ... & Zhu, R. (2020). *Advanced Materials*, *32*(39), 2002585.

41. Hu, M., Nie, R., Kim, H., Wu, J., Chen, S., Park, B. W., ... & Seok, S. I. (2021). *ACS Energy Letters*, *6*(10), 3555-3562.

42. Zhang, W., Li, X., Fu, S., Zhao, X., Feng, X., & Fang, J. (2021). *Joule*, *5*(11), 2904-2914.

43. Zhang, W., Liu, H., Qi, X., Yu, Y., Zhou, Y., Xia, Y., ... & Wang, H. L. (2022). *Advanced Science*, *9*(11), 2106054.

Supporting Information

Bidirectional Anions Gathering Strategy Afford Efficient Mixed Pb-Sn Perovskite Solar Cells

Yuli Tao[1,2#], Zheng Liang[1#], Jiajiu Ye[1#], Huifen Xu[1], Guozhen Liu[1], Dmitry Aldakov[3], Xu Pan[1], Peter Reiss,[3]* Xingyou Tian[1]**

1. Key Laboratory of Photovoltaic and Energy Conservation Materials, Institute of Solid-State Physics, Hefei Institutes of Physical Science, Chinese Academy of Science, Hefei 230031, China.

2. University of Science and Technology of China, Hefei 230026, China.

3. Univ. Grenoble Alpes, CEA, CNRS, INP, IRIG/SyMMES, STEP, 38000 Grenoble, France

E-mail: xpan@rntek.cas.cn, peter.reiss@cea.fr, xytian@issp.ac.cn

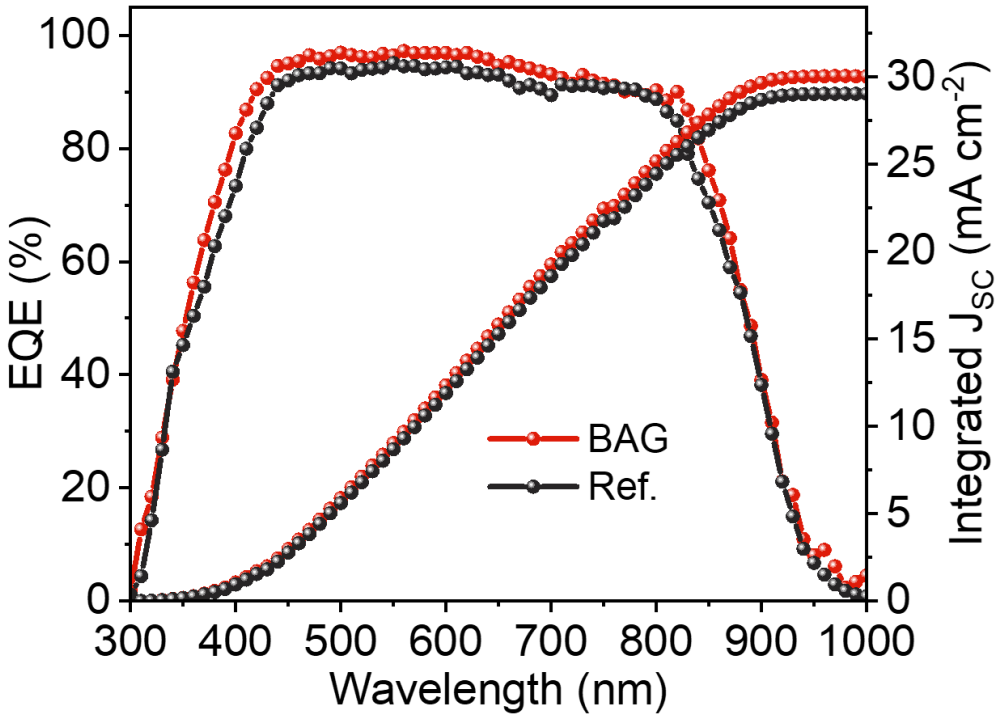

Figure S1. EQE spectra of reference device and BAG-devices. The integrated J_{SC} was 29.03 mA cm^{-2} and 30.05 mA cm^{-2} for the reference and BAG-devices, respectively.

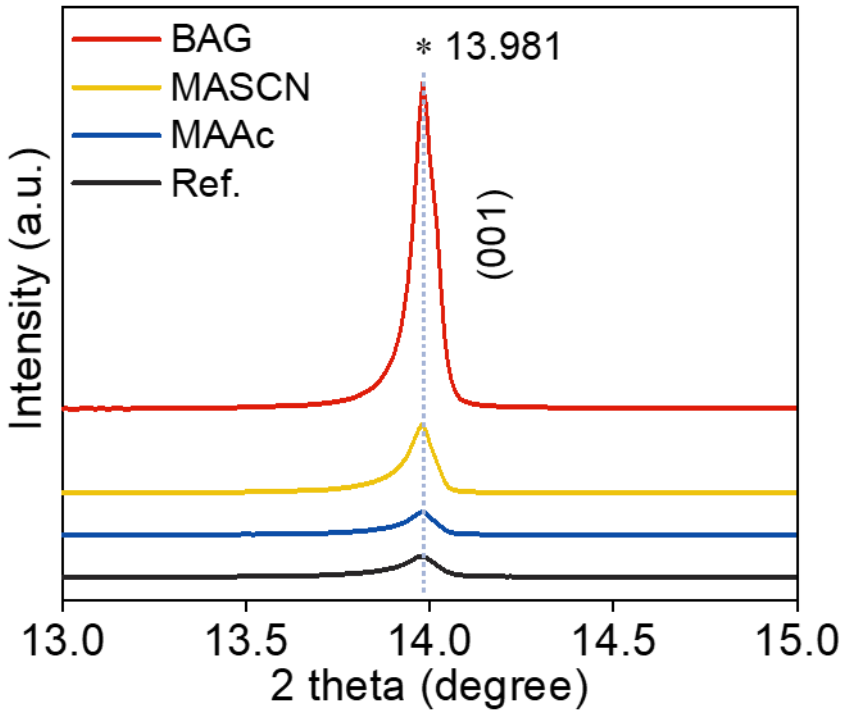

Figure S2. The XRD patterns of perovskite (001) peak treated by different additives. Neither shifts in the peaks, nor new peaks are observed in the XRD patterns.

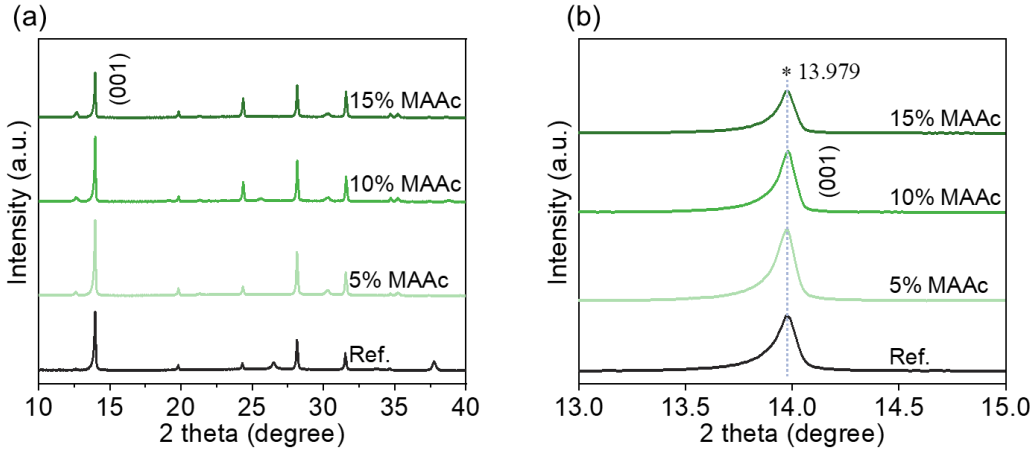

Figure S3. XRD patterns with various additive ratios of MAAc and corresponding (001) diffraction peaks.

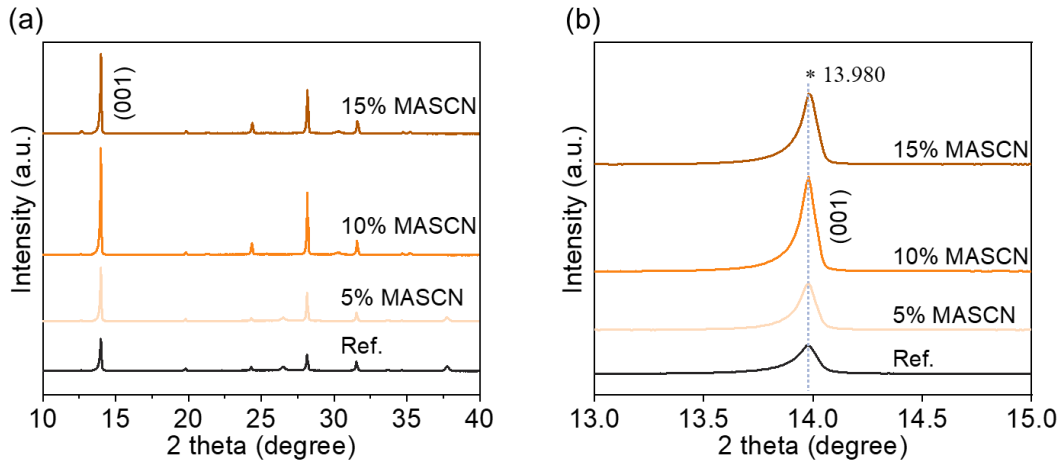

Figure S4. XRD patterns with various additive ratios of MASCN and corresponding (001) diffraction peak.

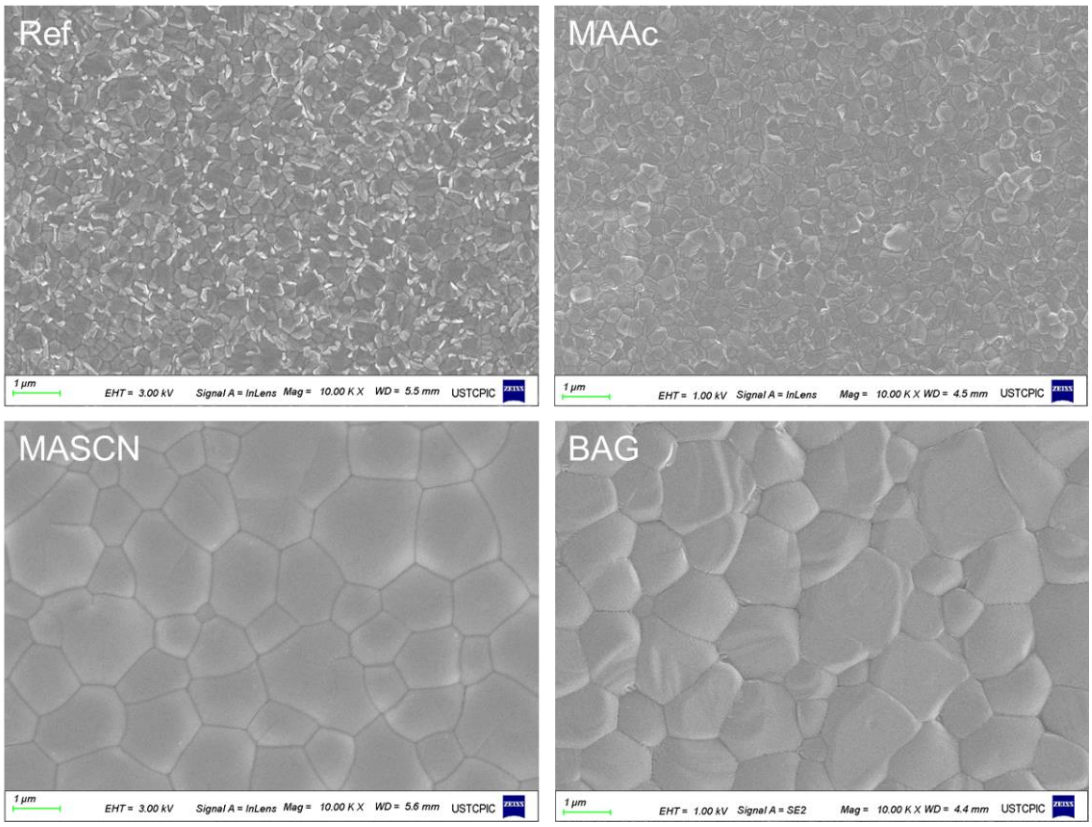

Figure S5. Top-view SEM images.

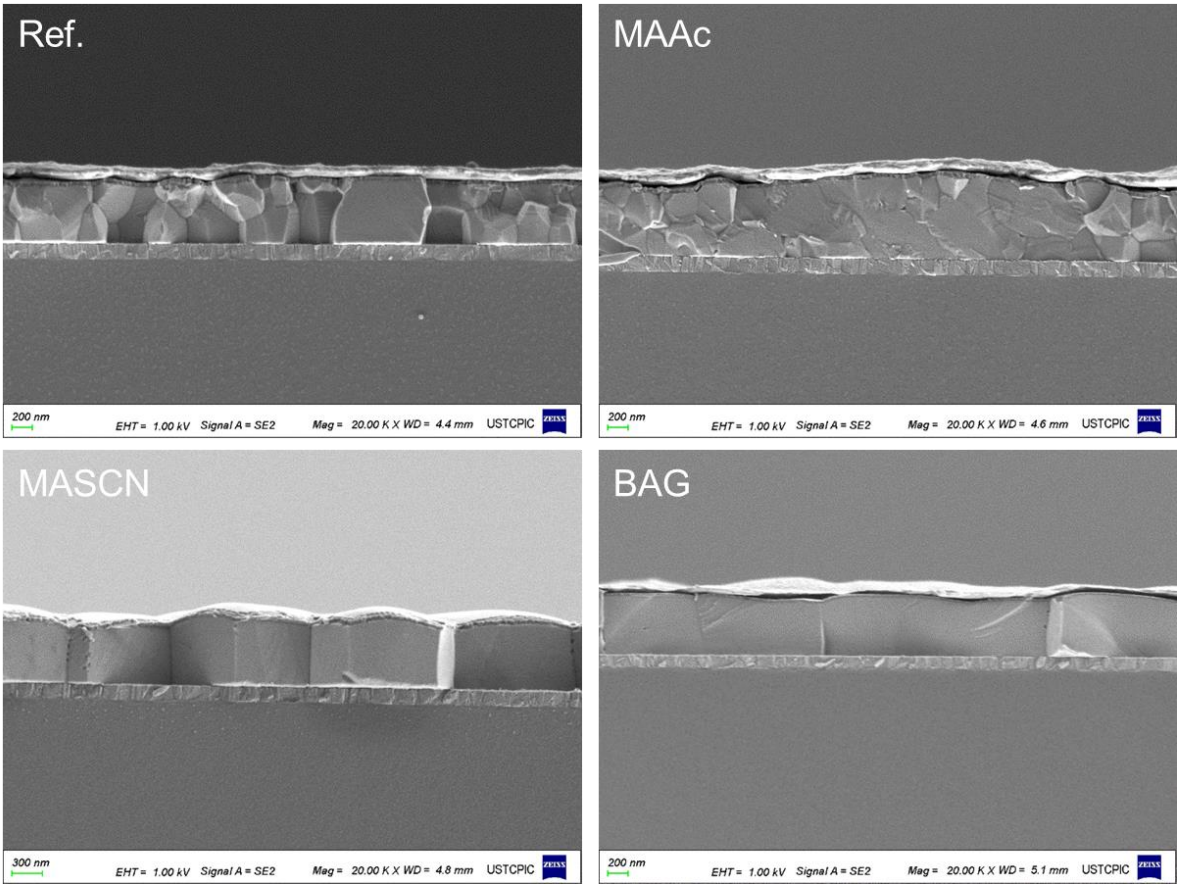

Figure S6. Cross-section SEM images.

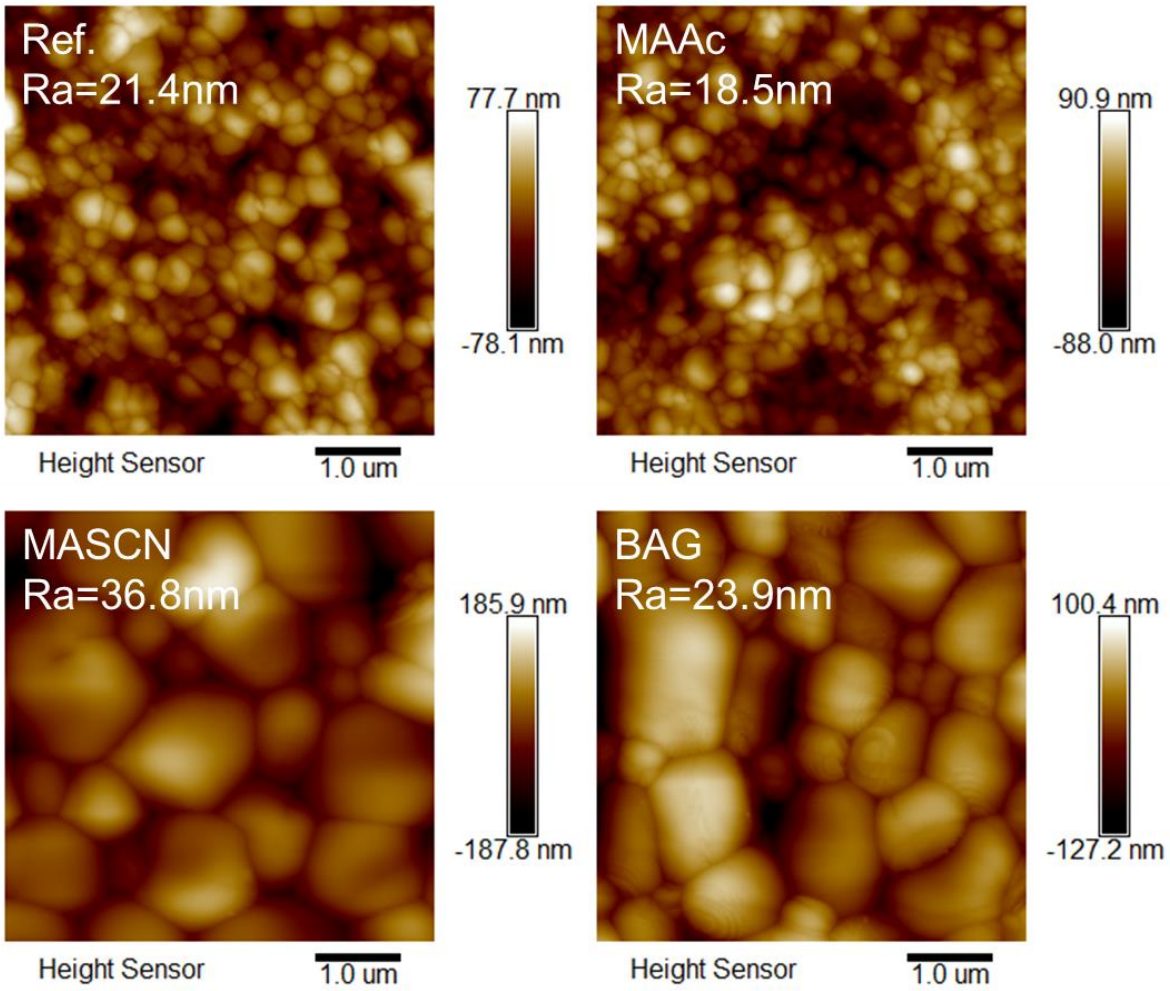

Figure S7. AFM images.

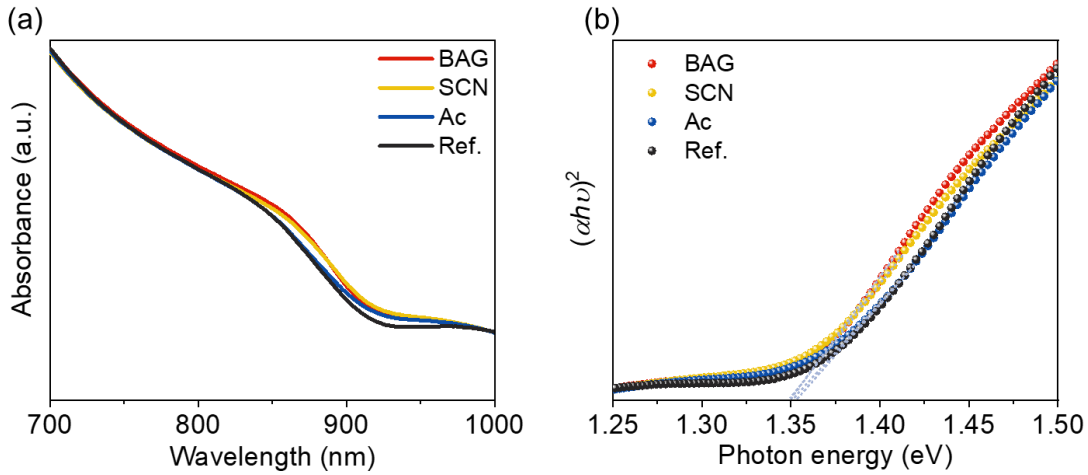

Figure S8. (a) UV-Vis spectra of perovskite film deposited on glass. (b) Tauc plot. In the Tauc-plot, the direct bandgap is determined by finding the intersection of a linear fit to $(\alpha E)^2$ with the abscissa in the acceptably linear range of $(\alpha E)^2$.

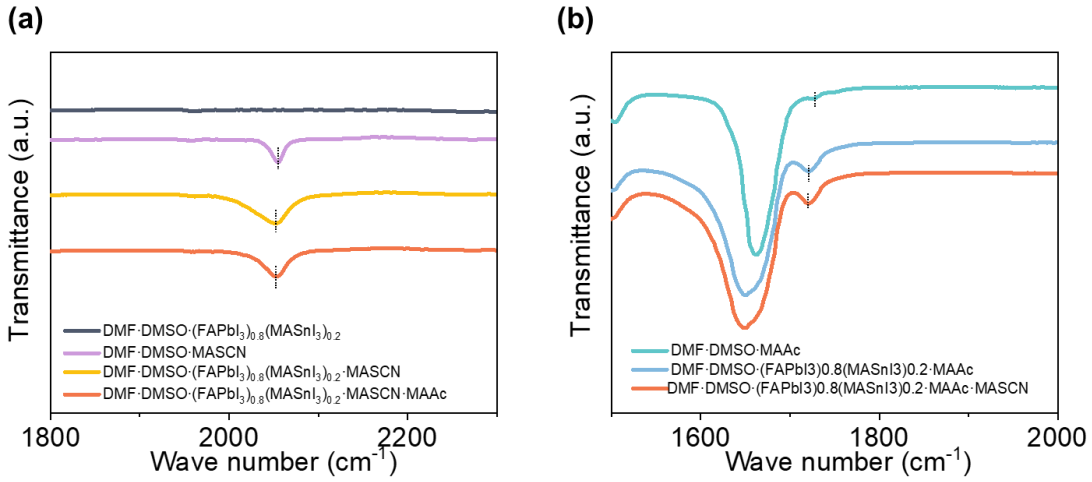

Figure S9. (a) FTIR spectra of solution for fingerprint regions of DMF·DMSO·$(FAPbI_3)_{0.8}(MASnI_3)_{0.2}$, DMF·DMMSO·MASCN, DMF·DMSO·$(FAPbI_3)_{0.8}(MASnI_3)_{0.2}$·MASCN, DMF·DMSO·$(FAPbI_3)_{0.8}(MASnI_3)_{0.2}$·MASCN·MAAc. (b) FTIR spectra of solution for fingerprint regions of DMF·DMSO·MAAc, DMF·DMSO·$(FAPbI_3)_{0.8}(MASnI_3)_{0.2}$·MAAc, DMF·DMSO·$(FAPbI_3)_{0.8}(MASnI_3)_{0.2}$·MAAc·MASCN.

NOTE: The shift of the characteristic peak in **Figure S9**a indicates the formation of a PbI_2·SCN adduct or SnI_2·SCN adduct. The shift of the characteristic peak in **Figure S9**b indicates the formation of a PbI_2·Ac adduct or SnI_2·Ac adduct. In addition, SCN- does not affect the formation of the Ac-relative-adduct, and Ac does not affect the formation of SCN-relative adduct.

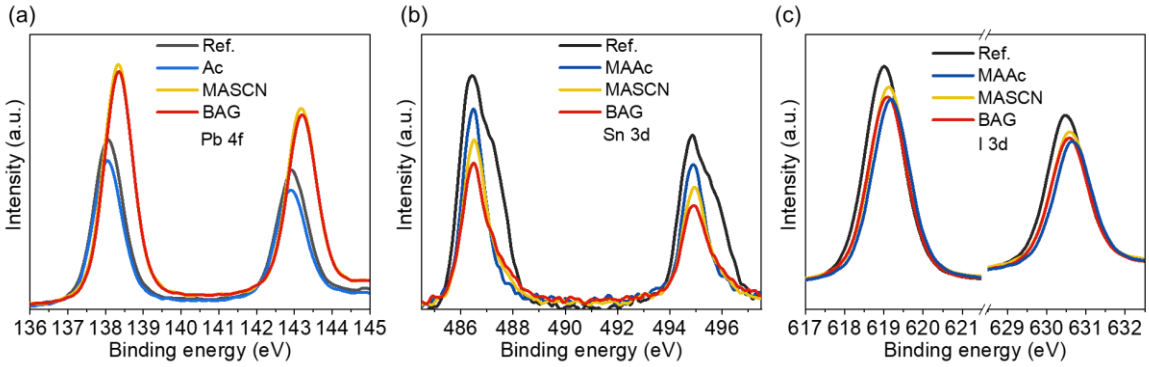

Figure S10. XPS spectra of Pb 4f (a), Sn 3d (b), I 3d (c).

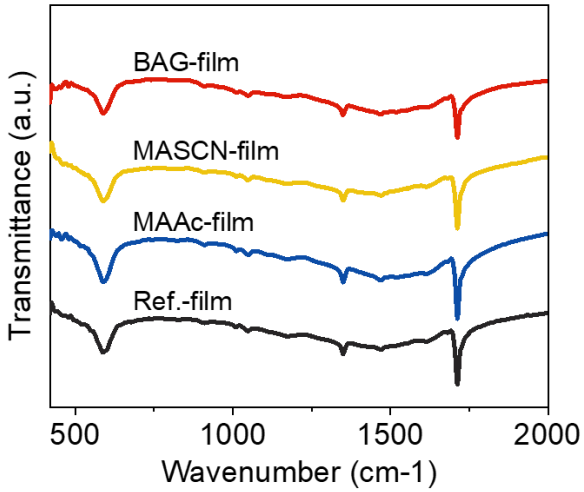

Figure S11. FTIR spectrograms of FTIR spectra for fingerprint regions of Ref.-film, MAAc-film, MASCN-film, and BAG-film.

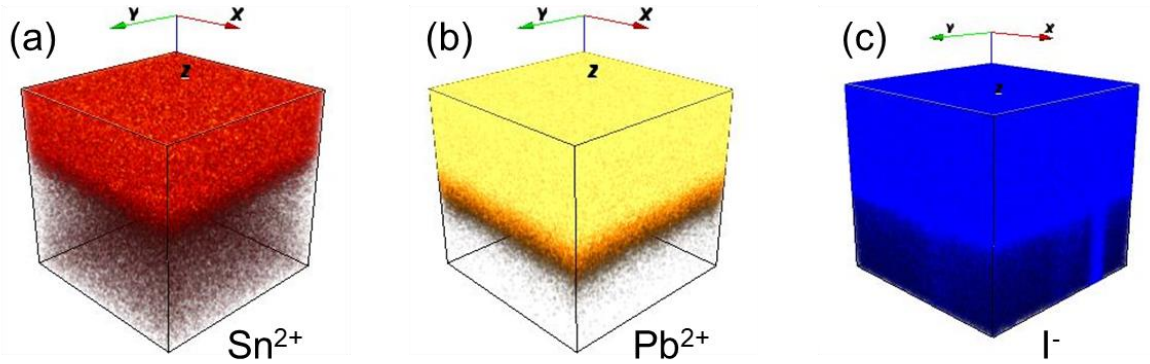

Figure S12. The 3D maps obtained from BAG-film show the distribution of (a) Sn^{2+}, (b) Pb^{2+}, and (c) I^-.

Support Table 1. The photovoltaic parameters of the reference, MAAc, MASCN, and BAG devices.

	V_{OC} (V)	J_{SC} (mA cm^{-2})	FF (%)	PCE (%)
BAG-Reverse	0.88	31.42	80.06	22.14
BAG-Forward	0.87	31.17	80.05	21.71
MASCN-Reverse	0.83	31.34	76.82	20.14
MASCN-Forward	0.82	31.35	74.18	19.25
MAAc-Reverse	0.78	30.67	79.89	19.24
MAAc-Forward	0.76	30.74	76.74	18.10
Ref.-Reverse	0.78	30.89	73.53	17.87

Ref.-Forward	0.70	30.35	74.38	15.85

Support Table 2. The specific parameters of TRPL.

	A1(%)	t1(ns)	A2(%)	t2(ns)	time(ns)
BAG	30.24708	72.17	69.75292	520.73	495.3004
MASCN	38.94496	45	61.05504	347.72	324.6363
MAAc	26.28179	34.79	73.71821	170.56	161.356
Ref.	64.92588	5.67	35.07412	95.59	86.69362